Int. J. Naval Archit. Ocean Eng. (2013) 5:1~20
http://dx.doi.org/10.2478/IJNAOE-2013-0114

Evaluation of sloshing resistance performance for LNG carrier insulation system based on fluid-structure interaction analysis

Chi-Seung Lee[1], Jin-Rae Cho[2], Wha-Soo Kim[1], Byeong-Jae Noh[1]
Myung-Hyun Kim[3] and Jae-Myung Lee[3]

[1]*Hyundai Heavy Industries Co., Ltd., Ulsan, Korea*
[2]*School of Mechanical Engineering, Pusan National University, Busan, Korea*
[3]*Department of Naval Architecture and Ocean Engineering, Pusan National University, Busan, Korea*

ABSTRACT: *In the present paper, the sloshing resistance performance of a huge-size LNG carrier's insulation system is evaluated by the fluid-structure interaction (FSI) analysis. To do this, the global-local analysis which is based on the arbitrary Lagrangian-Eulerian (ALE) method is adopted to accurately calculate the structural behavior induced by internal LNG sloshing of a KC-1 type LNG carrier insulation system. During the global analysis, the sloshing flow and hydrodynamic pressure of internal LNG are analyzed by postulating the flexible insulation system as a rigid body. In addition, during the local analysis, the local hydroelastic response of the LNG carrier insulation system is computed by solving the local hydroelastic model where the entire and flexible insulation system is adopted and the numerical analysis results of the global analysis such as initial and boundary conditions are implemented into the local finite element model. The proposed novel analysis techniques can potentially be used to evaluate the structural integrity of LNG carrier insulation systems.*

KEY WORDS: Hydroelastic analysis; FSI analysis; KC-1-type LNG carrier insulation system; Sloshing; ALE method; Global-local analysis.

INTRODUCTION

As the demand of natural resources such as natural gas and oil are tremendously increased, the huge size carrier such as liquefied natural gas (LNG) carrier is fabricated in nowadays. In accordance with this phenomenon, a lot of risk factors such as sloshing problem, crack propagation problem in midship section are emerged. Among these, the sloshing problem is considered as one of the most catastrophic problems since the structural failure of the LNG carrier leads to not only leakage of LNG but also tremendous loss of human and financial resources.

In order to overcome this problem, i.e., the insulation system which is consisted of lots of composites and austenitic stainless steels is adopted such as MARK-III-type, NO-96-type, KC-1-type insulation system. Among these, the KC-1-type insulation system which is fabricated by shipbuilding companies of Korea is designed to sustain the leakage of LNG as well as structural failure. Figs. 1 and 2 show the schematic of the membrane-type LNG carrier and the KC-1-type insulation system. This insulation system encounters the severe sloshing loads during its oversea operation. Hence, it is essential to guarantee the structural safety of the insulation system during its design and fabrication.

Corresponding author: *Jae-Myung Lee*
e-mail: *jaemlee@pusan.ac.kr*

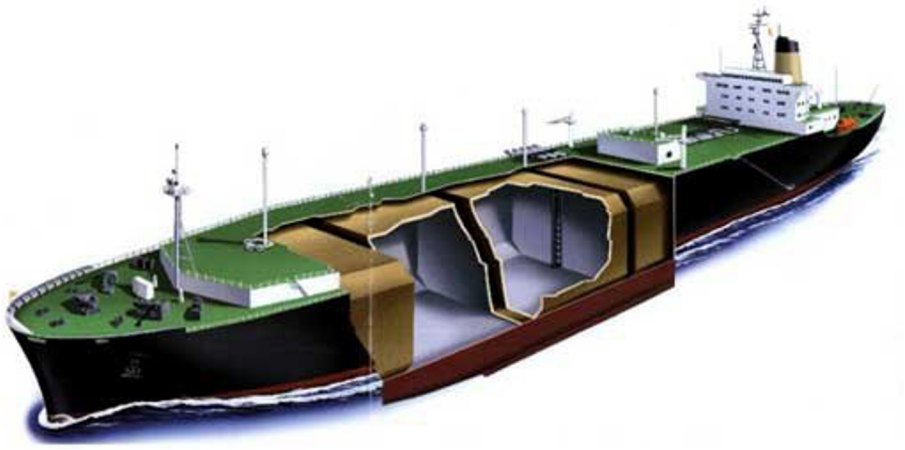

Fig. 1 Membrane-type LNG carrier with insulation system.

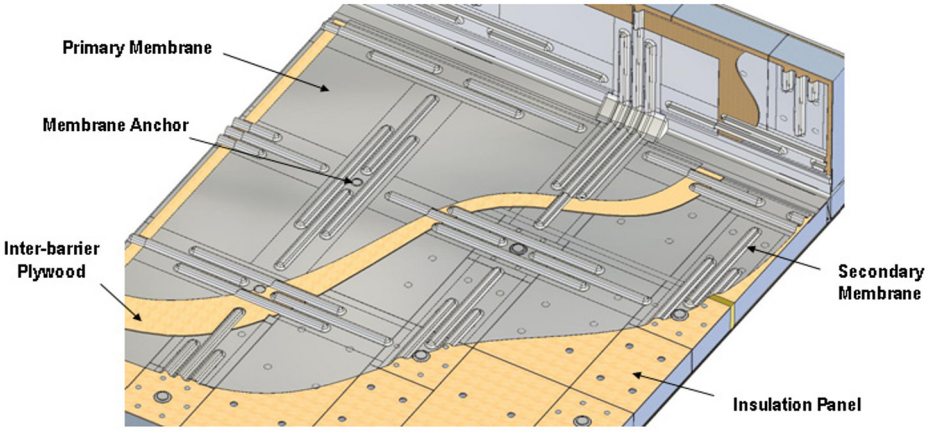

Fig. 2 Schematic of KC-1-type LNG carrier's insulation system.

For several decades, the hydroelastic analysis under sloshing has been analyzed by computational methods. In other words, the hydrodynamic pressure distributions as well as wave characteristics near the boundary condition are successfully evaluated based on finite element method (FEM) (Valtinsen, 1974; Nakayama and Washizu, 1980; Wu et al., 1998). However, in these researches, the structural response and behavior is not focused on, because the container is postulated as a rigid body and the interactive effect between interior fluid and exterior container is ignored. It is considered that the tremendous computational time and cost would be demanded when the structural deformations and interactive methods are adopted.

As an alternative method, the global-local basis fluid-structure interaction (FSI) analysis has gained attention for addressing the sloshing-induced structural response problem (Mote, 1971; Mao and Sun, 1991; Cho and Lee, 2003; Cho et al., 2008). In these researches, the structural behavior as well as correlation between internal LNG flow and external container can be considered in a unified formulation. On the other words, the sloshing-induced flow and hydrodynamic pressure can be obtained during the global analysis. In addition, the structural stress/strain and deformation can be estimated during the local analysis. In the process of the local analysis, the container is considered as a deformable body (not a rigid body) and boundary/initial conditions at an arbitrary time are implemented into the local analysis procedures. For this reason, the computational time and cost can be saved during the global-local analysis process.

Hence, in the present study, the global-local method based hydroelastic analysis which is successfully derived by Cho et al. (2008) has been adopted to evaluate the structural safety as well as hydrodynamic pressure induced by interior LNG flow for the KC-1-type LNG insulation system. During the global analysis, the flow motion characteristics such as the flow velocity, hydrodynamic pressure and volume fraction which are used as an initial and boundary condition for the local analysis are obtained. In addition, during the local analysis, the structural behaviors of the actual sized KC-1-type insulation system such as effective stress/strain and deformation are estimated precisely.

NUMERICAL MODELING OF HYDROELASTIC PROBLEM FOR LNG CARRIER'S INSULATION SYSTEM UNDER SLOSHING

Description of numerical modeling

The aforementioned hydroelastic problem has been analyzed by many scientists and engineers (Morand and Ohayon, 1995), especially Cho et al. (2008) who have successfully solved the hydroelastic problem of the MARK-III type LNG insulation system under sloshing. Prior to the FSI analysis for the KC-1-type LNG insulation system, the theoretical backgrounds such as problem descriptions, global-local analysis method are discussed in Chapter 2 based on the authors' previous study (Cho et al., 2008).

The hydroelastic response problem of the LNG carrier's insulation system is a representative example of the FSI problem, namely, the deformation of the insulation system (structure) is induced by LNG sloshing (fluid). Fig. 3 shows the LNG carrier's insulation system with length L, breadth B, height H, and thickness t. The fill ratio of LNG (i.e., volume of LNG with respect to insulation system internal volume) is defined as n_R. The insulation system is applied to external excitation during the operation.

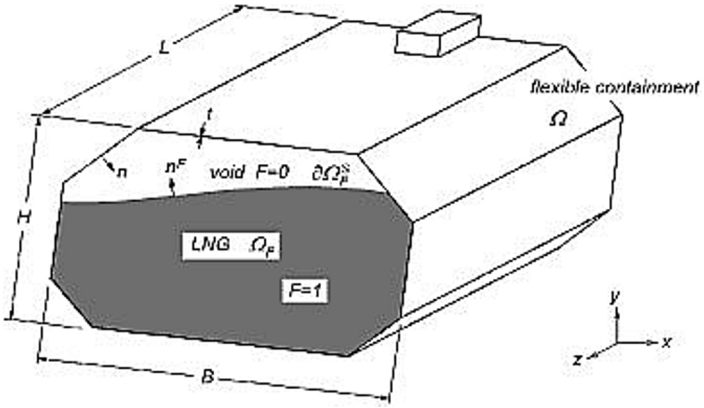

Fig. 3 Partially filled insulation system subjected to external excitation (Cho et al., 2008).

By considering the insulation system as a three-dimensional linear elasticity, the material and boundary domain can be written as $\Omega \in \mathbf{R}^3$ and $\partial\Omega = \overline{\partial\Omega_D \cup \partial\Omega_I}$, respectively, where $\partial\Omega_D$ is the essential boundary part and $\partial\Omega_I$ is the time-varying common interface contacting with interior LNG. The interface $\partial\Omega_D$ between the LNG and insulation system changes according to time. By neglecting the damping induced by the viscoelastic characteristics of the insulation ratio, the undamped dynamic displacement field $\mathbf{u}(\mathbf{x};t)$ is satisfied, and the initial and boundary condition can be represented as

$$\sigma_{ij}(\mathbf{u})_{,j} + \rho(f_i - \ddot{u}_i) = 0 \quad \text{in} \quad \Omega \times (0,T] \tag{1}$$

$$\mathbf{u}(\mathbf{x};0) = \mathbf{u}^0(x), \quad \dot{\mathbf{u}}(\mathbf{x};0) = \dot{\mathbf{u}}^0(\mathbf{x}) \tag{2}$$

$$\mathbf{u}(\mathbf{x};t) = \hat{\mathbf{u}}(\mathbf{x};t) \quad \text{on} \quad \partial\Omega_D \times (0,T] \tag{3}$$

$$\sigma_{ij}(\mathbf{x};t) n_j n_i = -p(\mathbf{x};t) \quad \text{on} \quad \partial\Omega_I \times (0,T] \tag{4}$$

where σ_{ij} is the Cauchy stress and ρ and f are the density and body force of the insulation system, respectively, p is the hydrodynamic pressure caused by LNG, $\mathbf{n}$ is the normal unit vector in boundary $\partial\Omega$, and T is the analysis time section. $\mathbf{u}^0$ and $\dot{\mathbf{u}}^0$ are the initial value of the displacement and velocity fields, respectively. $\hat{\mathbf{u}}$ denotes the displacement constraint by the rigid dummy closure, which moves by the rigid body motion of the global rigid container.

The LNG domain transformed into the movement of the free surface $\partial\Omega_F^S$ can be expressed as $\Omega_F \in \mathbf{R}^3$. Moreover, for hydroelastic analysis of the LNG movement in the insulation system, the effects of viscosity and temperature change can be neglected due to the large amount of internal volume; hence, the sloshing of LNG can be considered as incompressible and inviscid. Therefore, the velocity of fluid $\mathbf{V}(\mathbf{x};t)$ can be written as follows.

$$\nabla \cdot \mathbf{V} = 0 \quad \text{in} \quad \Omega_F \times (0,T] \tag{5}$$

The momentum equation can be written as follows.

$$\rho_F \frac{\partial \mathbf{V}}{\partial t} + \rho_F (\mathbf{V} \cdot \nabla)\mathbf{V} = \nabla \cdot \sigma^F \quad \text{in} \quad \Omega_F \times (0,T] \tag{6}$$

The initial and boundary conditions of Eqs. (5) and (6) can be represented as

$$\mathbf{V}(\mathbf{x};0) = 0 \tag{7}$$

$$\mathbf{V}(\mathbf{x};t) \cdot \mathbf{n}^F = \frac{\partial \mathbf{u}}{\partial t} \cdot \mathbf{n}^F \quad \text{on} \quad \partial\Omega_I \times (0,T] \tag{8}$$

$$\sigma_{ij}^F n_j^F = t_i^F \quad \text{on} \quad \partial\Omega_F^S \tag{9}$$

where ρ_F is the density of LNG, $\mathbf{u}(\mathbf{x};t)$ is the displacement of the insulation system, $\mathbf{n}^F$ is the normal unit vector with regard to the flow boundary, and $\partial\Omega_I$ and $\partial\Omega_F^S$ are the boundaries of the insulation system and free surface of LNG, respectively. The traction $\hat{t}^F$ acting on the LNG-free boundary disappears when the flow is assumed to be inviscid (Cho and Lee, 2003). The total stress tensor of LNG σ^F can be written as $\sigma^F = -p\mathbf{I}$, where p is the hydrodynamic pressure of fluid and $\mathbf{I}$ is the unit tensor.

The flow boundary can be used to obtain the transport equation and its initial condition; namely,

$$\frac{\partial F}{\partial t} + \mathbf{V} \cdot \nabla F = 0 \quad \text{in} \quad \Omega_F \times (0,T] \tag{10}$$

$$F(\mathbf{x};0) = F_{ini}(\mathbf{x}) \tag{11}$$

where F_{ini} is the initial value of the volume fraction F. According to the Eulerian kinematic description, the volume fractions of the LNG and void are 1 (LNG flow region) and 0 (void region), respectively.

Global-local analysis technique

In order to analyze the structural response of complex structures, a huge number of degrees of freedom are needed; hence, a large amount of computational time and cost is required. Thus, it is impossible to obtain the structural response for the entire structure as a whole. The global-local analysis technique was introduced as an alternative method to investigate the structural response of regions of interest in structures (Mote, 1971; Mao and Sun, 1991). In global-local analysis, the global analysis is carried out prior to the local analysis. The finite element (FE) model is simplified to save the calculation time. By using approximate mechanical information of the global structures such as the reaction force, the displacement can be obtained. Based on this information, local analysis of the region of interest is then performed. In local analysis, the FE model is fabricated as a real structural/material model, and specific mechanical information of specific regions can finally be acquired. The global-local

analysis technique is widely used in the structural analysis of complex structures due to its reliable analysis results and efficient computational time/cost.

Fig. 4 shows the global-local approach for the hydroelastic analysis. The structural response of the right-top corner region of the LNG insulation system was investigated at critical time t_c. Fig. 4(a) shows the simplified global rigid-insulation system sloshing model. The goal of the global analysis was to find the primary mechanical information of the rigid-insulation system sloshing problem: the total flow field $\mathbf{V}_G(\mathbf{x};t)$, pressure field $p_G(\mathbf{x};t)$ and volume fraction $F_G(\mathbf{x};t)$ of the internal LNG (Cho and Lee, 2004). These global analysis results can be used as an initial condition for the local analysis. Fig. 4(b) shows the local flexible hydroelastic model, which consists of the locally flexible insulation system domain Ω^L and local LNG domain Ω_F^L.

In local hydroelastic analysis, the continuity and momentum equations can be written as

$$\nabla \cdot \mathbf{V}_L = 0 \quad \text{in} \quad \Omega_F^L \times (0, T^\tau] \tag{12}$$

$$\rho_F \frac{\partial \mathbf{V}_L}{\partial \tau} + \rho_F (\mathbf{V}_L \cdot \nabla)\mathbf{V}_L = \nabla \cdot \sigma_L^F \quad \text{in} \quad \Omega_F^L \times (0, T^\tau] \tag{13}$$

where $\mathbf{V}_L$ is the flow velocity within the local flow region Ω_F^L with the local boundary $\partial\Omega_F^L$ and σ_L^F is the total stress in local region. The initial and boundary conditions can be represented as follows.

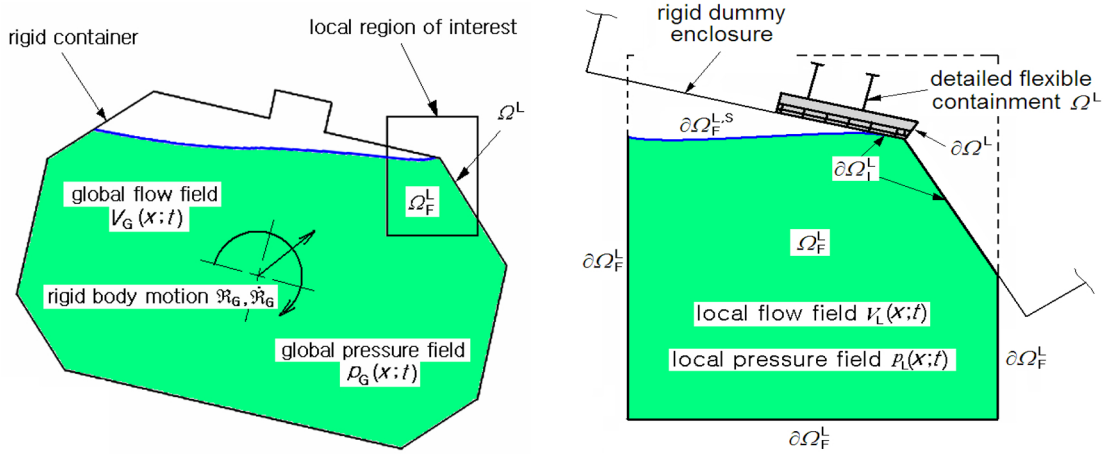

(a) (b)

Fig. 4 Global-local approach for hydroelastic analysis: (a) global rigid-insulation system sloshing model and (b) local flexible hydroelastic model (Cho et al., 2008).

$$\mathbf{V}_L(\mathbf{x};0) = \mathbf{V}_G(\mathbf{x};t_c), \quad p_L(\mathbf{x};0) = p_G(\mathbf{x};t_c) \tag{14}$$

$$\mathbf{V}_L(\mathbf{x};\tau) \cdot \mathbf{n}^F = \frac{\partial \hat{\mathbf{u}}_L}{\partial \tau} \cdot \mathbf{n}^F \quad \text{on} \quad \partial\Omega_I^L \times (0, T^\tau] \tag{15}$$

The transport equation and its boundary condition can be written as

$$\frac{\partial F_L}{\partial \tau} + \mathbf{V}_L \cdot \nabla F_L = 0 \quad \text{in} \quad \Omega_F^L \times (0, T^\tau] \tag{16}$$

$$F_L(\mathbf{x};0) = F_G(\mathbf{x};t_c) \tag{17}$$

where T^{τ} is the total analysis time in local analysis and τ is the time section $t-t_c$ and F_L is the local volume fraction. $\tilde{\mathbf{u}}_L$ is the displacement of the dummy-rigid insulation system model. T^{τ} is the very short time during the global analysis time T, and the surface tension effect in the free surface $\partial\Omega_F^{L,S}$ can be ignored due to the assumption of inviscid flow.

The undamped displacement $\mathbf{u}_L$ of the flexible local model, which has a boundary condition of $\partial\Omega = \overline{\partial\Omega_D^L \bigcup \partial\Omega_I^L}$, where $\partial\Omega_D$ is the essential boundary part in local domain and $\partial\Omega_I$ is the time-varying common interface contacting with interior LNG in local region, can be written as follows.

$$\sigma_{ij}^L(\mathbf{u}_L)_{,j} + \rho(f_i - \ddot{u}_i^L) = 0 \quad \text{in} \quad \Omega^L \times (0, T^{\tau}] \tag{18}$$

The initial and boundary conditions of the above equation can be expressed as

$$\mathbf{u}_L(\mathbf{x};0) = \mathbf{R}_G(\mathbf{x};t_c), \quad \dot{\mathbf{u}}_L(\mathbf{x};0) = \dot{\mathbf{R}}_G(\mathbf{x};t_c) \tag{19}$$

$$\mathbf{u}_L(\mathbf{x};\tau) = \hat{\mathbf{u}}_L(\mathbf{x};\tau) \quad \text{on} \quad \partial\Omega_D^L \times (0, T^{\tau}] \tag{20}$$

$$\sigma_{ij}^L(\mathbf{x};\tau) n_j^L n_i^L = -p_L(\mathbf{x};\tau) \quad \text{on} \quad \partial\Omega_I^L \times (0, T^{\tau}] \tag{21}$$

where $\mathbf{R}_G(\mathbf{x};t_c)$ and $\dot{\mathbf{R}}_G(\mathbf{x};t_c)$ are the displacement and velocity, respectively, of the local insulation system Ω^L by rigid-insulation system motion at critical time t_c. $\hat{\mathbf{u}}_L(\mathbf{x};\tau)$ is the displacement constraint by the rigid shell dummy. As shown in Fig. 4, the rigid shell dummy moves along the rigid insulation system motion.

Numerical approximation for FVM-FEM coupling

Eqs. (12), (13), and (16) can be represented by a generalized form, that is,

$$\frac{\partial}{\partial\tau}(\Lambda\Phi) + \frac{\partial}{\partial x_j}(\Lambda V_j^L \Phi) = S_{\Phi} \quad \text{in} \quad \tilde{\Omega}_F^L \times (0, T^{\tau}] \tag{22}$$

where Φ is the dependent variable, Λ is the coefficient, S_{Φ} is the source term dependent on the governing equation, and $\tilde{\Omega}_F^L$ is the extended Euler region including the void region within the local insulation system. In other words, $\Phi=1$, $\Lambda=\rho_F$, and $S_{\Phi}=0$ in the continuity equation; $\Phi=V_j^L$, $\Lambda=\rho_F$ and $S_{\Phi}=-\partial p_L/\partial x_j$ in the momentum equation; and $\Phi=F_L$, $\Lambda=1$, and $S_{\Phi}=0$ in the volume fraction equation, respectively. In this study, the three-dimensional finite volume method (FVM) was adopted for space discretization, and the first-order Eulerian scheme was applied for the spatial discretization and the time integration of the three transport equations, respectively. The extended Eulerian domain $\tilde{\Omega}_F^L$ is discretized into a finite number of non-overlapping control volume, and the time period T^{τ} is divided into N time intervals $\Delta\tau = T^{\tau}/N$ with $N+1$ time stages $\tau_n = n\Delta\tau\,(n=0,1,2,\cdots,N)$.

Fig. 5(a) shows the three-dimensional control volume of grid point P and the six neighboring grid points. The volume and surface of the control volume are δV and A, respectively. By integrating Eq. (22) with regards to the control volume δV and time increment $\Delta\tau$ and by applying the divergence theorem, next equation can be obtained to solve the working variable Φ_P^{n+1} at time stage τ_{n+1}.

$$\Lambda\frac{\delta V}{\Delta\tau}(\Phi_P^{n+1} - \Phi_P^n) + \int_A \Lambda V_j^L \Phi^{n+1} n_j^L ds = \bar{S}_{\Phi} \tag{23}$$

Here, $\bar{S}_{\Phi}$ is the volume integral of the source term S_{Φ}.

$$\overline{S}_\Phi = \int_{\delta V} S_\Phi dV = \overline{S}_C + \overline{S}_P \Phi_P^n \tag{24}$$

where $\overline{S}_C$ is the part of $\overline{S}_\Phi$ independent of Φ, $\overline{S}_P$ is the coefficient of Φ_P, and $\overline{S}_C$ and $\overline{S}_P$ are the coefficients at arbitrary time step τ_n.

From Eq. (24), the discretized formula to obtain the variable Φ_P^{n+1} at time step τ_{n+1} can be written as

$$a_P \Phi_P^{n+1} = \sum_{nb} a_{nb} \Phi_{nb}^{n+1} + \overline{S}_C + a_P^0 \Phi_P^n, \quad a_P = \sum_{nb} a_{nb} + a_P^0 - \overline{S}_P \tag{25}$$

where $a_P^0 = \Lambda \delta V / \Delta \tau$. a_{nb} is the function of the dependent variable. This variable is different from that of the discretization theory and remeshing. In this study, the power scheme was adopted to describe the spatial variation approximation (Patankar, 1980).

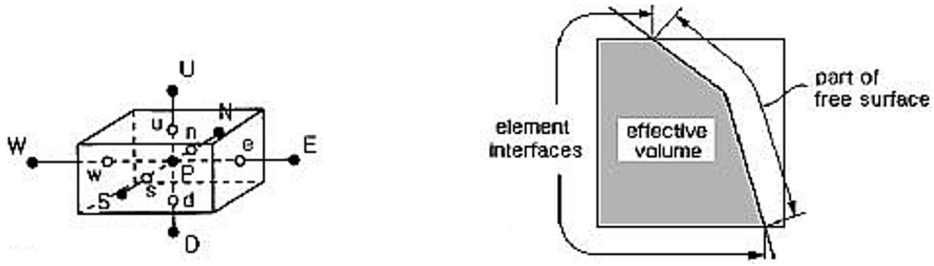

(a) (b)

Fig. 5 Schematic representation of (a) three-dimensional control volume element and (b) the effective volume and boundary of an element intersecting with the free surface (Cho et al., 2008).

The momentum equations in the discretized linear algebraic equations system, i.e., Eq. (25) are firstly solved to compute time-step-wise flow velocities using the initial conditions or the previous time-level values. It is evident from Fig. 5(b) that volume and surface integrals of the partially filled elements are carried out over the effective volume and the effective boundary, respectively, where the effective boundary consists of the element interfaces and the part of the fluid free surface.

On the other hand, the calculated velocities do not satisfy the continuity equation, hence, the pressures should be adjusted in each control volume element occupied by the fluid. From Fig. 6(a), the element-centered pressure p_C at the free surface and the pressure p_N of one of the neighboring elements inside the fluid can be written as

$$p_C = (1-\eta) p_N + \eta p_S \tag{26}$$

with $\eta = d_C / d$. The neighbor element should be chosen such that the line connecting the centers of control elements is closest to the normal to the free surface (Hirt and Nichols, 1981).

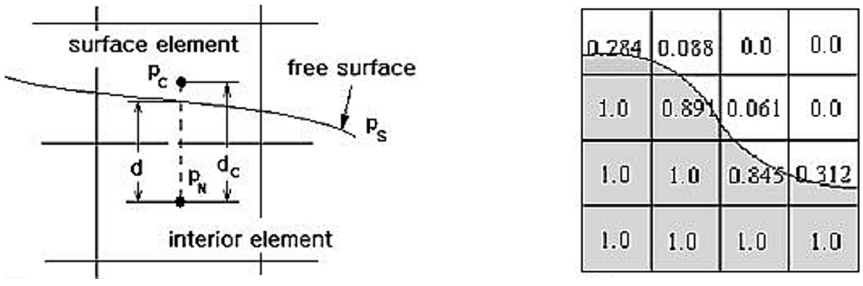

(a) (b)

Fig. 6 Schematic representation of (a) pressure interpolation for an element intersecting with the free surface and (b) free surface interpolation within the extended Euler domain (Cho et al., 2008).

Once the pressure and velocity fields are calculated, the volume fraction equation in the discretized linear algebraic equation system, i.e., Eq. (25) is calculated to compute the element-wise constant volume fraction as shown in Fig. 6(b). In addition, in order to maintain the computational stability, the time-step size should not exceed the critical value given by

$$\Delta t \le h/(c+u) \tag{27}$$

where c is the speed of sound in fluid, u is the flow velocity, and h is the smallest distance between two adjacent element centers.

By applying the isotropic finite element approximation technique to Eq. (18), the undamped displacement field $\mathbf{u}_L$ can be represented as follows.

$$\mathbf{u}_L(\mathbf{x};\tau) = \Phi(\mathbf{x}) \cdot \bar{\mathbf{u}}_L(\tau) \tag{28}$$

where $\bar{\mathbf{u}}_L$ is the undamped displacement field regarding to only one variable, and in the present study, the variable is time (Zienkiewicz et al., 2005). As a result, the following matrix equations can be acquired.

$$\mathbf{M}\ddot{\mathbf{u}}_L + \mathbf{K}\mathbf{u}_L = \mathbf{F} \tag{29}$$

where $\mathbf{F}$ is the load vector by gravity and hydrodynamic pressure; this is written as follows.

$$\mathbf{F} = \int_{\Omega^L} \Phi^T(\rho\mathbf{f})dV + \int_{\partial\Omega_f^L} \Phi^T \mathbf{p}_L ds \tag{30}$$

The time integration is carried out based on the central difference method (explicit method) and/or Newmark method (implicit method). However, the explicit method is widely adopted in dynamic structural problems of huge/complex structures due to the reduction of analysis time (Hu, 1997). The local analysis time T^τ can be divided by the detail intervals of the finite numbers. The equation of motion (Eq. (29)) can then be replaced by the explicit time increment form such as through the following equation according to the lumped mass matrix $\tilde{\mathbf{M}}$.

$$\ddot{\bar{\mathbf{u}}}_L^n = \tilde{\mathbf{M}}^{-1}(\mathbf{F}^n - \mathbf{K}\bar{\mathbf{u}}_L^n) \tag{31}$$

According to the central difference method and dynamic relaxation method, which is based on the α-damping method, the velocity and displacement of each time step are derived as

$$\dot{\bar{\mathbf{u}}}_L^{n+1/2} = (1-\alpha)\dot{\bar{\mathbf{u}}}_L^{n-1/2} + \Delta\tau\ddot{\bar{\mathbf{u}}}_L^n \tag{32}$$

$$\bar{\mathbf{u}}_L^{n+1} = \bar{\mathbf{u}}_L^n + \Delta\tau\dot{\bar{\mathbf{u}}}_L^{n+1/2} \tag{33}$$

where $\alpha \cong 1.67\omega_{\max}\Delta\tau$. The size of the time increment step is properly decided from the following formula to consider the convergence and stability of the numerical analysis.

$$\Delta\tau \le (2/\omega_{\max}) \tag{34}$$

where $\omega_{\max}$ is the largest element frequency in the finite element mesh (Cho et al., 2006; Cho et al., 2007).

On the other hand, in the local hydroelastic problem, the LNG flow and structural motion influence each other at the common surface $\partial\Omega_I^L$. These physical interactions must satisfy the following kinematic and contact stress constraints (Schäfer and Teschauer, 2001).

$$\mathbf{V}_L \cdot \mathbf{n}^F = \dot{\tilde{\mathbf{u}}}_L \cdot \mathbf{n}^F \quad \text{on} \quad \partial\Omega_I^L \tag{35}$$

$$\sigma_{ij}^{L,F} n_j^F = \sigma_{ij}^L n_j^F \quad \text{on} \quad \partial\Omega_I^L \tag{36}$$

The fluid-structure constraints can be numerically represented by direct standardization and the iterative discretized method. Applying the former method to complex structures is extremely difficult. Therefore, the latter method was adopted for this study. The two kinds of equations (i.e., fluid domain and structure domain governing equations) are separately calculated by using the iterative discretized method, and the interaction of the fluid and structure is calculated alternately. In order to overcome the mismatch of the mesh, the projection method was also adopted (Farhat et al., 1998).

In the local analysis for this study, the fixed Eulerian mesh was used for the LNG flow, and the complex and dense mesh was used for structures. In this case, the incompatible Eulerian-Lagrangian interaction method can be used effectively. As shown in Fig. 7(a), the fluid mesh is larger than the physical domain of LNG, and the active and inactive domains are separated by the common interface $\partial\Omega_I^L$. On the other hand, the dummy-rigid insulation system coupled model is implemented to the fixed Eulerian mesh, and its closed outer surface serves as a coupling surface Γ. In general in the Euler-Lagrange coupling, the coupling surface should be closed and set larger than the common fluid-structure interface, namely, $\Gamma \supset \partial\Omega_I^L$.

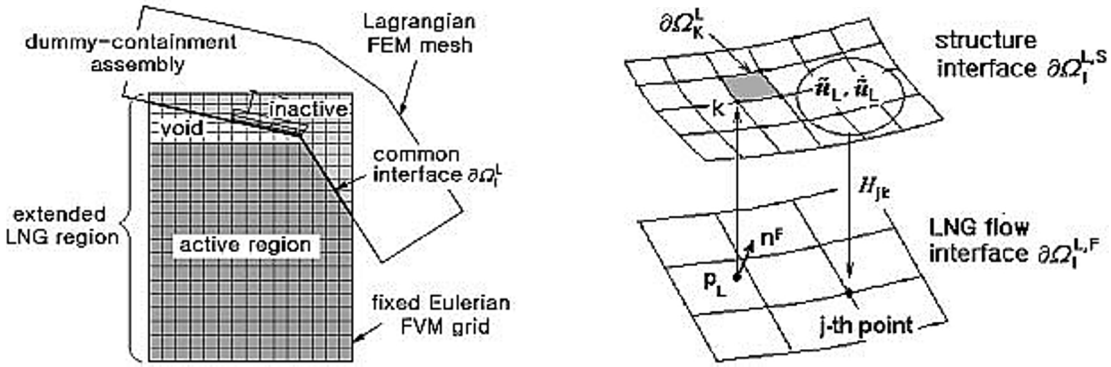

(a) (b)

Fig. 7 Schematic of (a) incompatible Eulerian-Lagrangian coupling and (b) transfer through non-matching fluid-structure interface (Cho et al., 2008).

In order to transfer the hydrodynamic pressure p_L of the flow field to the structure and the displacement $\tilde{\mathbf{u}}_L$ and velocity $\dot{\tilde{\mathbf{u}}}_L$ of the structure to the flow field, the related variables must be interpolated. In this study, the structure mesh was denser than the fluid mesh; hence, the mesh pattern and basic function of the structure can be used as a standard mesh to interpolate the related variables. As shown in Fig. 7(b), the surface force $t_F^L\big|_{\partial\Omega_K^L}$, which is transferred to the surface element $\partial\Omega_K^L$ of the structure interface $\partial\Omega_I^{L,S}$, is implicitly interpolated as n numbers of shape functions ψ_k, which is defined at the two-dimensional master element $\hat{\Omega}$.

$$(t_F^L)_i\big|_{\partial\Omega_K^L} = \sum_{k=1}^{n} \psi_k(\hat{\mathbf{x}})(p_{L,k} n_i^k), \quad \hat{\mathbf{x}} \in \hat{\Omega} \tag{37}$$

where $p_{L,k}$ is the pressure at node k above the structure interface $\partial\Omega_I^{L,S}$ which is transferred from $\partial\Omega_I^{L,F}$ and $\hat{\Omega}$ is the two-dimensional master element.

The displacement and velocity of structure are transferred to the flow field using the incompatibility interpolation method (Harder and Desmarais, 1972). Here, note that the former adjusts the flow boundary of LNG, whereas the latter one specifies the flow boundary condition given in Eq. (15). In Fig. 7(b), j and k represent the j th node of $\partial\Omega_I^{L,F}$ and k th node of $\partial\Omega_I^{L,S}$. Eq. (35), that is, the kinematic constraint, can be written as follows using the H coupling matrix (Beckert, 2003).

$$(\mathbf{V}_L \cdot \mathbf{n}_F)_j = \sum_{k=1}^{m} H_{jk} (\dot{\tilde{\mathbf{u}}}_L \cdot \mathbf{n}^F)_k \tag{38}$$

The coupling in time can be done using either explicit or implicit approach, and the flowchart of the analysis algorithm in both approaches is presented in Fig. 8 (Cho et al., 2008). Based on the analysis algorithm, the user-defined subroutine is programmed. In this study, the explicit time coupling for the current problem with the critical time-step size determined by Eq. (27)

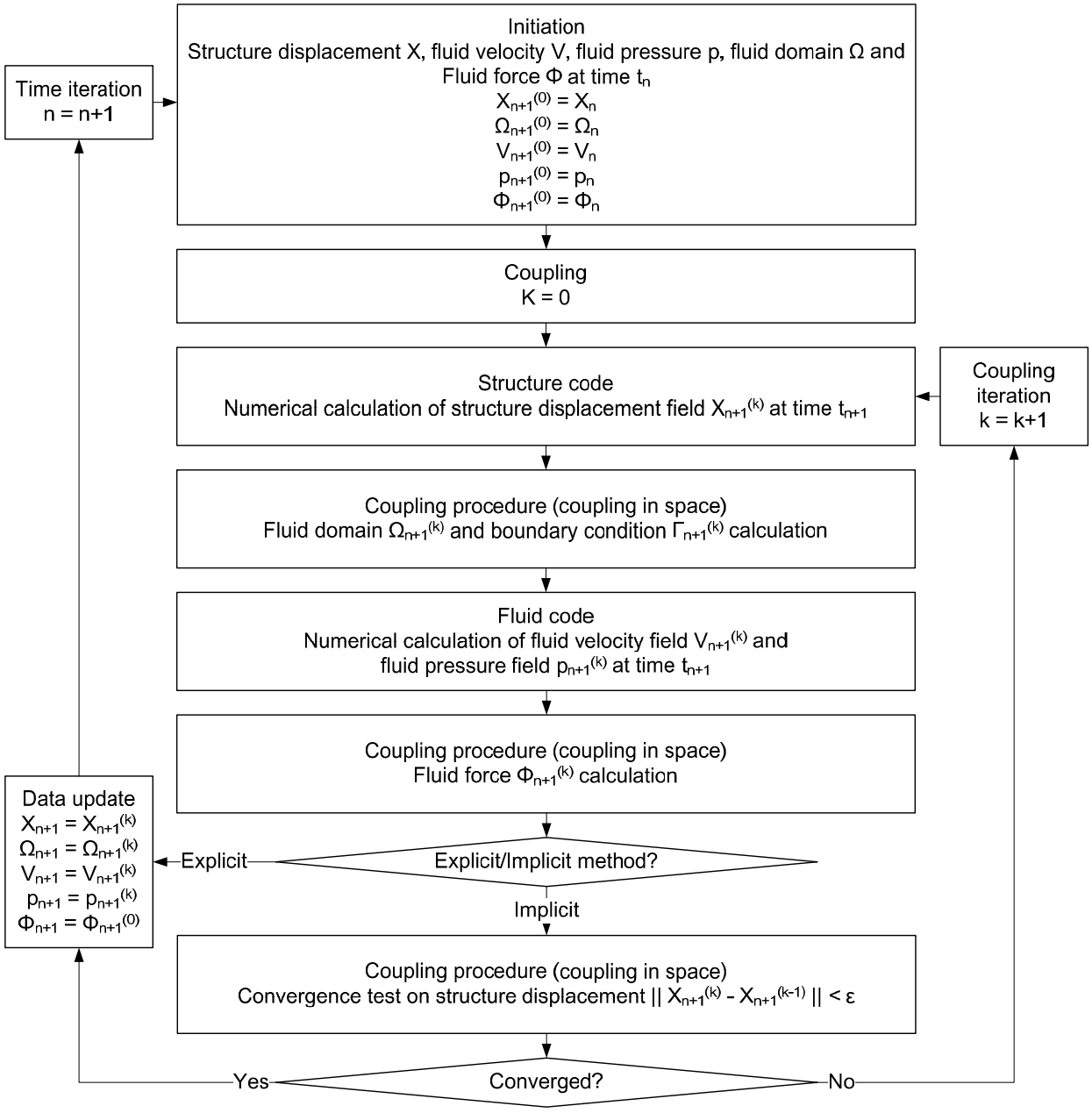

Fig. 8 Explicit and implicit fluid-structure coupling methods (Sigrist and Abouri, 2006; Cho et al., 2008).

and (34). The numerical implementation of the local staggered hydroelastic analysis using the explicit incompatible Eulerian-Lagrangian coupling method is carried out as follows.

(1) The initial structure-LNG interface $\partial\Omega_I^L$ in the local model is specified and the initial free surface $\partial\Omega_F^{L,S}$ is defined by assigning the volume fraction F_L to each local Eulerian cell.
(2) Based on initial and boundary conditions, i.e., Eqs (19)-(21), the structural dynamic equation system, namely, Eq. (18) is time integrated to solve the displacement $\mathbf{u}_L$ and the velocity $\dot{\mathbf{u}}_L$ of the local flexible insulation system.
(3) Next, the LNG interface $\partial\Omega_I^{L,F}$ is moved by $\mathbf{u}_L$ and specified with $\dot{\mathbf{u}}_L$ as the interface flow boundary condition, i.e., Eq. (15) according to non-matching interpolation scheme, namely, Eq. (38).
(4) Based on the adjusted active LNG material boundary, the flow boundary conditions and the initial condition, i.e., Eq. (14), the transport equations (Eq. (22)) are solved to find the local flow velocity $\mathbf{V}_L$, the volume fraction F_L, and the hydrodynamic pressure p_L.
(5) The free surface $\partial\Omega_F^{L,S}$ and the structure-LNG interface $\partial\Omega_I^L$ are updated, and then the LNG hydrodynamic p_L is transferred to the structure interface $\partial\Omega_I^{L,S}$. And then, go to the next time integration.

DESCRIPTIONS OF KC-1 TYPE INSULATION SYSTEM FE MODELS

FE models

Figs. 9 and 10 show the local FE model and its component for the KC-1 type LNG carrier's insulation system. Fig. 11(a) shows the dummy element used as an interface, and Fig. 11(b) shows the coupled interface between the dummy and the membrane of the insulation system. The mechanical properties and element type of the KC-1 type FE model are shown in Table 1.

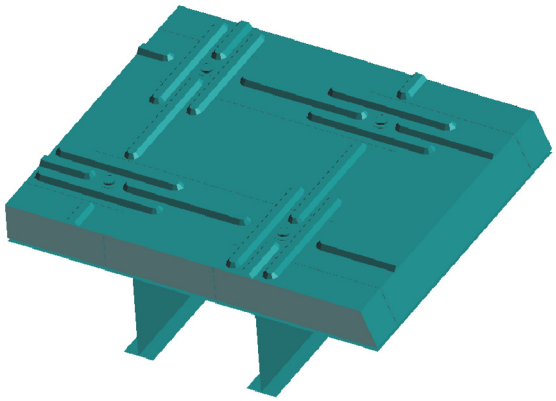

Fig. 9 Local model of KC-1 type LNG carrier's insulation system.

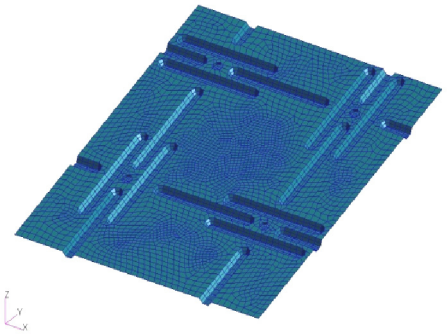

(a) Membrane.

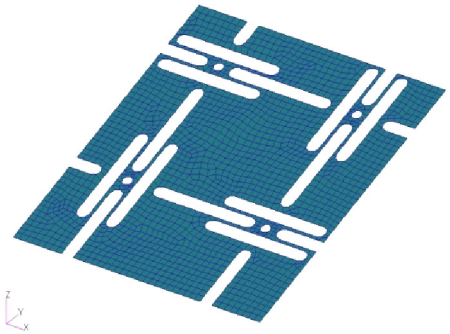

(b) New plywood.

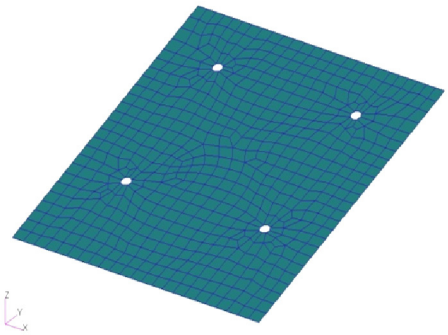

(c) Top plywood.

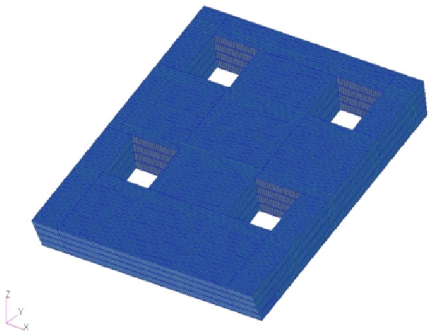

(d) R-PUF.

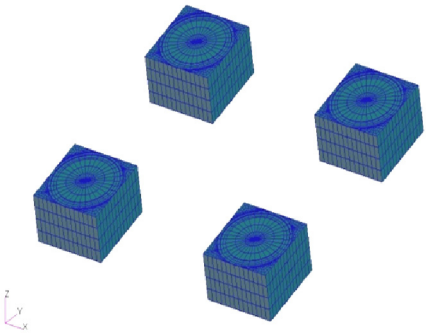

(e) Anchor and supports.

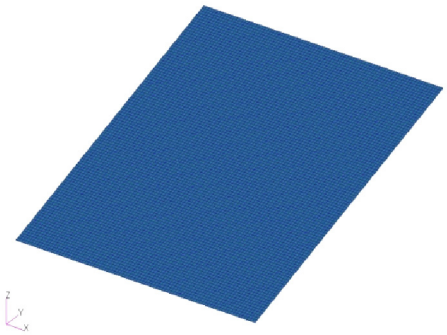

(f) Bottom plywood.

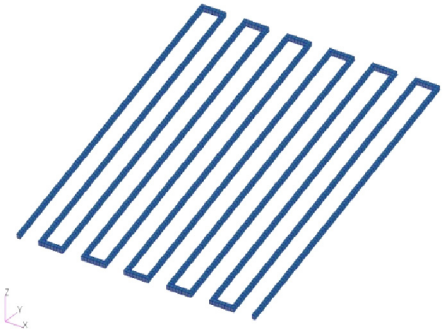

(g) Mastic.

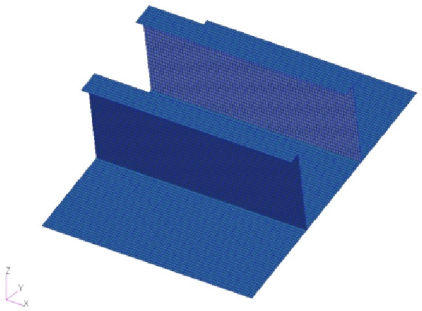

(h) Hull.

Fig. 10 Components of KC-1 LNG carrier's insulation system.

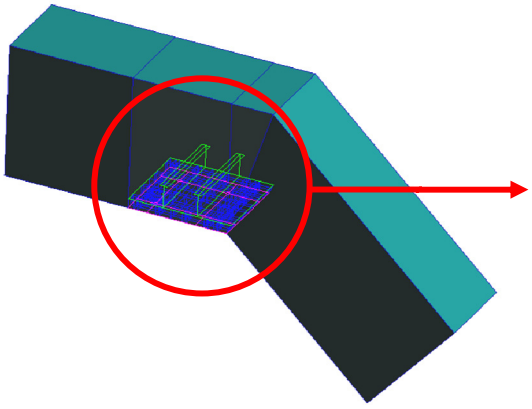

(a) Dummy model.

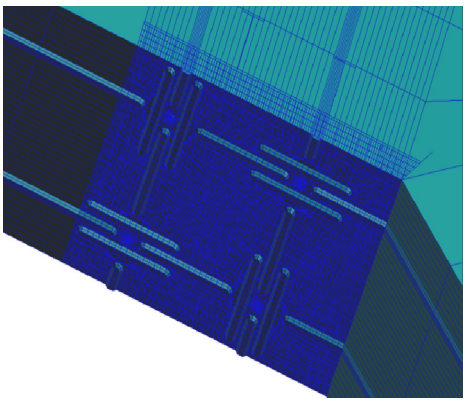

(b) Coupling surface.

Fig. 11 Construction of coupling surface for KC-1 type local model.

Table 1 Material properties and element type of KC-1 type model.

Parts	Element types	Material properties	Values
Membrane	DMATEP - shell element (Elastoplastic material)	ρ (Density)	7850 kg/m^3
		E (elastic modulus)	200 *GPa*
		ν (Poisson's ratio)	0.27
		t (thickness)	1.2 *mm*
Plywood	DMATEP - shell element (Elastoplastic material)	ρ (Density)	710 kg/m^3
		E (elastic modulus)	8.2 *GPa*
		ν (Poisson's ratio)	0.17
		t (thickness) (top, bottom)	(9, 12) *mm*
R-PUF	DMATOR - Lagrangian element (Orthotropic elastic material)	ρ (Density)	125 kg/m^3
		(E_1, E_2, E_3)	(131, 131, 50) *MPa*
		(ν_1, ν_2, ν_3)	(0.2, 0.153, 0.153)
		(G_{12}, G_{23}, G_{13})	(12.2, 12.2, 12.2) *MPa*
		t (thickness) (top, bottom)	(120, 150) *mm*
Triplex	DMATEP - shell element (Elastoplastic material)	ρ (Density)	2500 kg/m^3
		E (elastic modulus)	13.133 *GPa*
		ν (Poisson's ratio)	0.3
		t (thickness)	1, 2, 3 *mm*
Mastics	DMATEL - Lagrangian element (Isotropic elastic material)	ρ (Density)	2500 kg/m^3
		E (elastic modulus)	2.87 *GPa*
		ν (Poisson's ratio)	0.3
		t (thickness)	10 *mm*
Hull	DMATEP - shell element (Elastoplastic material)	ρ (Density)	7850 kg/m^3
		E (elastic modulus)	206 *GPa*
		ν (Poisson's ratio)	0.3
		t (thickness)	10 *mm*
LNG	DMAT - Eulerian element (General material)	ρ (Density)	500 kg/m^3
		K (bulk modulus)	1.44 *GPa*

Boundary conditions

Fig. 12 shows the boundary conditions of the dummy-local KC-1 insulation system model. If node sharing is applied to this model, the stress concentration may occur on the interface between the dummy and local model. In other words, the model types of the dummy and local models are rigid and deformable, respectively. Hence, the mismatch in deformation can cause an abnormal increase of stress. In order to overcome this problem, the contact element was adopted between the two models used in this study.

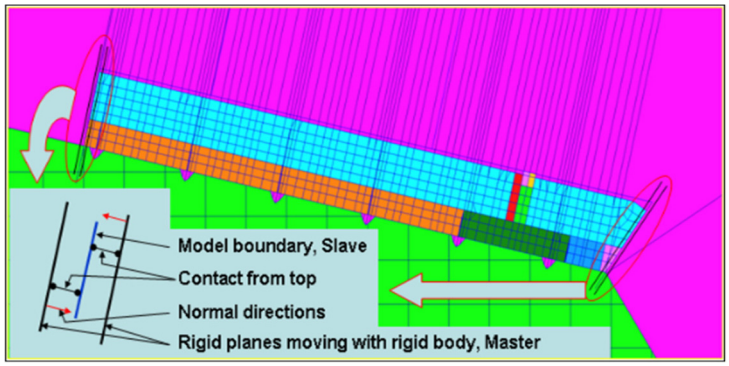

Fig. 12 Construction of coupling surface for KC-1 type local model.

Simplified FE model for anchor section

An anchor section exists between the insulation system and hull. The anchor combines the R-PUF and membrane firmly. The surface of the anchor is made of SUS 304L, and inside is filled with R-PUF. The implemented position and lamination structure of the anchor is shown in Fig. 13.

The anchor has extremely complex lamination structures, as well as others, and it might be necessary to create a mesh that is quite fine. However, this could induce a huge amount of calculation time to analyze the anchor region. In order to save the computational time and cost, the simplified FE model of the anchor section was introduced in this study. The two kinds of analysis scenarios were adopted as shown in Fig. 14.

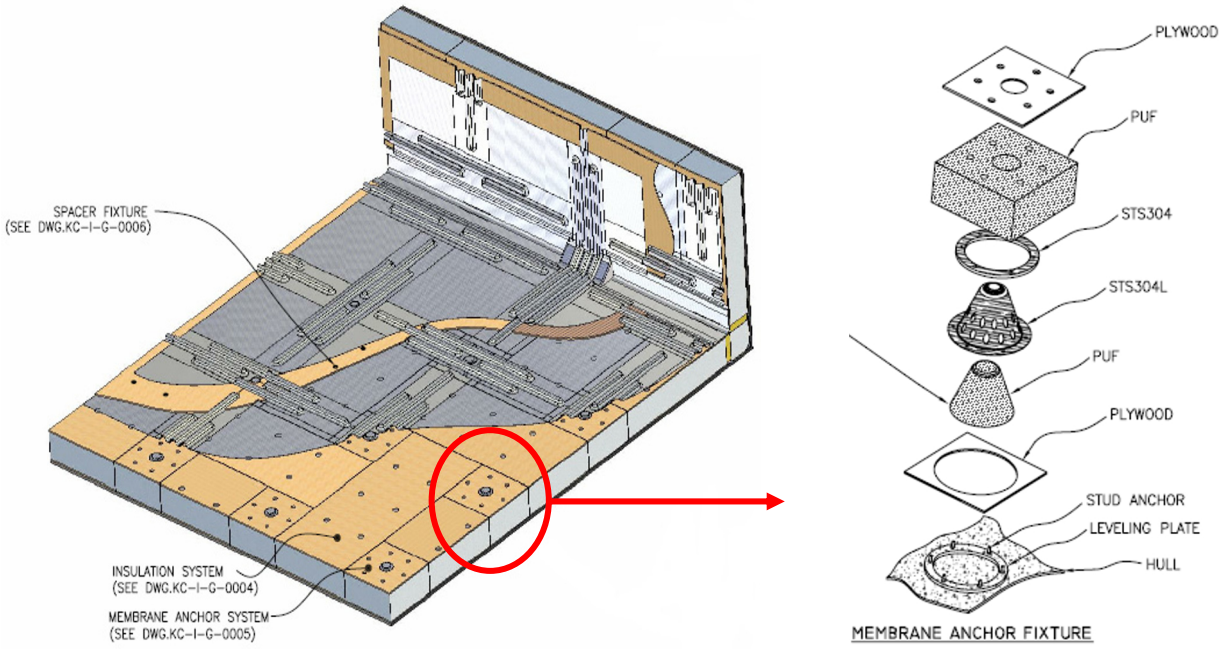

Fig. 13 Implemented position and lamination structure of anchor.

Case A is the general FE model, which was fabricated by using element refinement. The connection area between the membrane and anchor was established as surface-to-surface contact. On the other hand, in Case B, the upper side of the anchor was eliminated for fast calculation. Instead, the additional thickness model with a coarser mesh size than the as-is model was implemented to the upper side of the anchor. In addition, this model was unified with the membrane FE model. By using the additional thickness model, the calculation time can be improved. Moreover, the modeling time can be reduced due to the absence of the contact element. The related description such as number of elements and computational time will be discussed in Chapter 4.

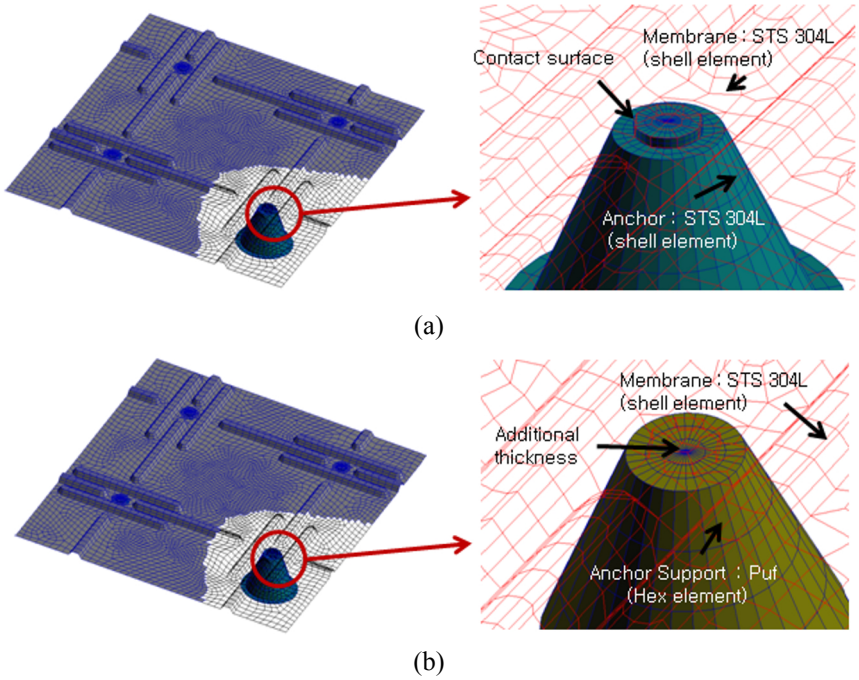

Fig. 14 Anchor model types: (a) Case A (fine mesh model) and (b) Case B (simplified model).

GLOBAL-LOCAL HYDROELASTIC ANALYSIS RESULTS AND DISCUSSIONS

Global analysis

Fig. 15 shows the FE model of the LNG carrier insulation system for global analysis. The dimensions of the FE model were 42.84 *m* × 37.4 *m* × 27.2 *m* (length × breadth × height). The filling level (η_R), density (ρ_F), and bulk modulus (K) of the LNG were 95%, 500 *kg/m*^{3}, and 1.44 *GPa*, respectively. The FE model was fabricated based on a control volume element (Euler domain) and bilinear rigid shell element (Lagrangian domain). The numbers of each element are 135,608 and 48,366, respectively, as shown in Fig. 15(a). The analysis was carried out using MSC. Dytran and the interfaces between the LNG flow and rigid insulation system were fabricated using the arbitrary Lagrangian Eulerian (ALE) method.

The insulation system was applied to a sinusoidal rolling excitation as shown in Fig. 15(b). The angular velocity was defined as $\dot{\theta}_Z(t) = a\omega\cos(\omega t)$, and the amplitude and the angular frequency were defined as a=3.87° and ω=2π/5.5 *rad/sec*, respectively, based on the actual measurement data in the shipping service. The rolling starts with the extremely small excitation until 5 *sec* for the simulation purpose of the huge and heavy insulation system.

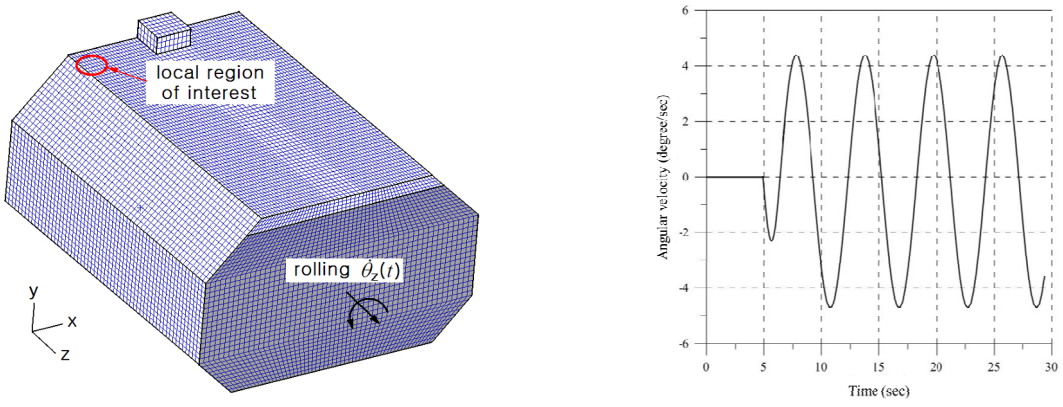

(a) (b)

Fig. 15 LNG insulation system in rolling motion: (a) rigid insulation system model and (b) sinusoidal rolling excitation.

The computational analysis time was set to 0 *sec* to 4014 *sec* based on the actual measured data of the target LNG carrier. In the case of this target LNG cargo tank, the critical situation was occurred once per approximately 4000 *sec*. The averaged time increment and the corresponding number of iterations were $\overline{\Delta t} = 3.598 \times 10^{-3}$ *sec* and 1,115,508, respectively.

Fig. 16(a) and (b) show the volume fraction distribution and the sloshing flow of interior LNG at time 4010 *sec*. At this time, the insulation system inclined 12° in the clockwise direction. The choice of the critical time itself is not a main interest considering the goal of the present study, but the critical time was selected from the fact that the local region of concern is subjected to the remarkable hydrodynamic impact when the LNG sloshing flow is going up along the inner surface of the insulation system. It can be clearly seen that the rigid tank sloshing produces high LNG flow along the inner boundary of the insulation system, particularly at all the corners of the insulation system (Cho et al., 2008). According to the detailed numerical data, the peak flow velocity and the peak hydrodynamic pressure at the critical time are 1.26 *m/s* and 0.142 *MPa*, respectively.

It is noted that the insulation system experiences the peak rolling amplitude equal to 22.1° in the rigid tank sloshing. Although the excitation from 5 to 30 *sec* is small and looks like not changeable as shown in Fig. 15(b), the cargo tank as well as LNG carrier are rolled to approximately 22° due to sloshing and ship motion coupling phenomenon. This has been already discussed by a few naval architects such as Faltinsen and Timokha (Faltinsen and Timokha, 2009). In their study, the increase of the ship motion amplitude is experimentally investigated and related governing equations are derived. Moreover, the concept of the anti-rolling ship is also proposed by controlling the coupling between sloshing and ship motion. In the present study, this coupling phenomenon is also observed during the simulation (global analysis).

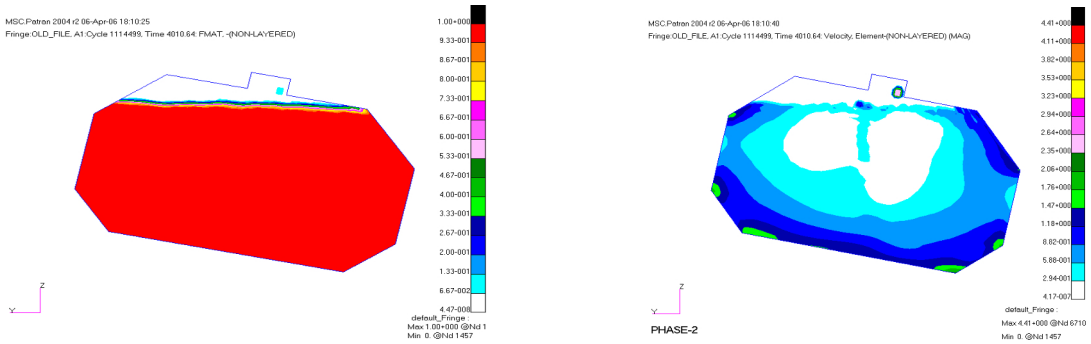

(a) (b)

Fig. 16 Global analysis results at t = 4010 *sec*: (a) LNG volume fraction and (b) LNG flow (unit: *m/s*).

Fig. 17 shows the mapping of the LNG flow into the local problem region Ω_F^L. The global flow velocity field $\mathbf{V}_G(\mathbf{x};t_c)$ and the global hydrodynamic pressure field $p_G(\mathbf{x};t_c)$ of the finite volume mesh of the global model were mapped into the finite volume mesh of the local model. If the free surface is totally positioned in the internal/external region of the control volume, the volume fraction F_L is 1 or 0. The value of the volume fraction is decided as $0 < F_L < 1$ according to the position of the free surface. The three kinds of calculated data (i.e., velocity field, pressure field, and volume fraction) were applied to the initial conditions of Eqs. (12)-(17). The fluid field mesh of the fine local model consisted of 31589 uniform control volumes; the mechanical values of ρ_F and K used for LNG in the local model were the same as the values from the global analysis results.

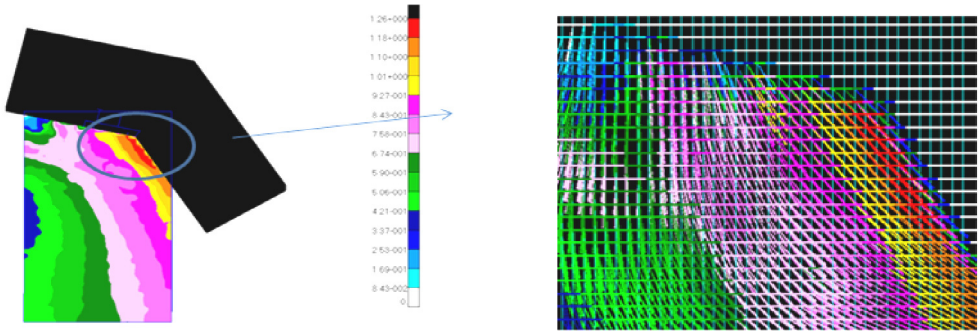

(a) (b)

Fig. 17 Mapping of the LNG flow into the local problem region: (a) global view, (b) detailed view.

Local analysis

Based on the data of the global analysis results, the local analysis was carried out. Figs. 18 and 19 show the local analysis results of the effective stress contour regarding Cases A and B. In both cases, the maximum effective stress occurred in the membrane region at $35ms$. The specific value of the maximum effective stress is listed in Table 2. In addition, the computational times for Case A and B are shown in Table 3. As shown in these tables, the differences between each case were found to be quite small and the computational time of the proposed FE model (Case B) is much less than the as-is FE model (Case A); therefore, it is reasonable to choose the Case B type anchor model during local analysis.

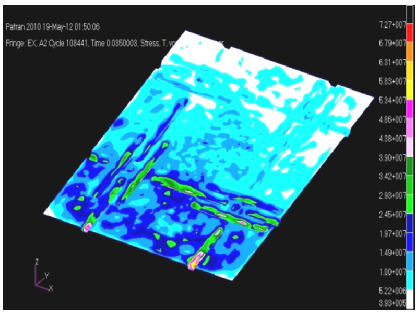

(a) Membrane.

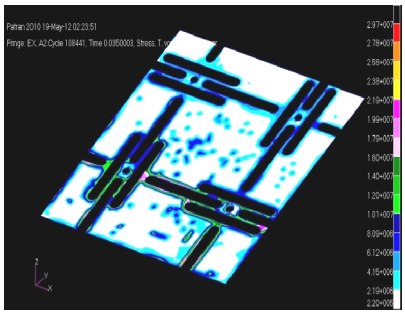

(b) New plywood.

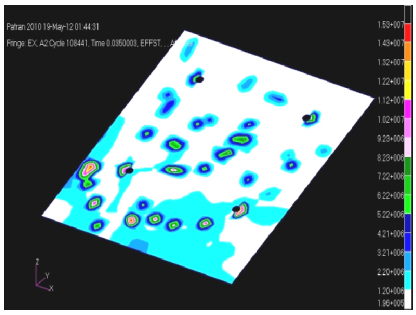

(c) Top plywood.

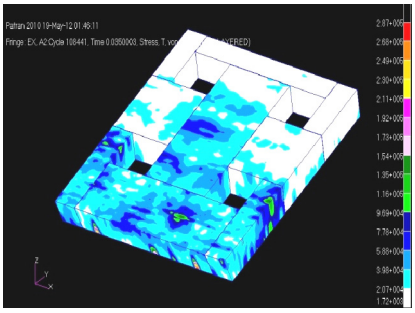

(d) R-PUF.

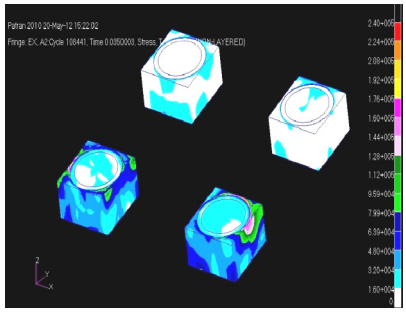

(e) Anchor and supports.

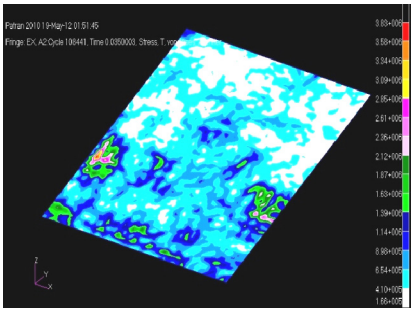

(f) Bottom plywood.

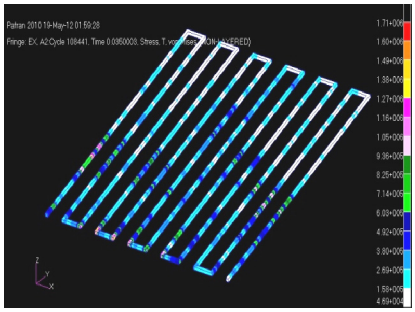

(g) Mastic.

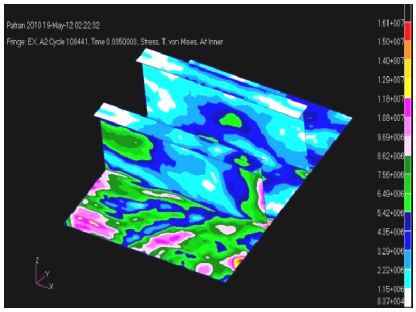

(h) Hull.

Fig. 18 Effective stress contour of KC-1 model Case A.

Through Table 2, it is confirmed that the average stress value of Case B is bigger (but not much) than the value of Case A. It is considered that this phenomenon might be caused by the differences of element types, i.e., shell-contact element type in Case A and shell-hexahedral element type in Case B. However, these differences can be acceptable considering the computational time and cost as shown in Table 3. In this table, it can be found that the CPU time of Case A is much bigger than the Case B. Since it takes huge time to calculate the interface and contact regions in the Case A FE model. Hence, it is confirmed that the proposed FE model is more time and cost effective case when the FSI analysis of the LNG carrier cargo tank is carried out.

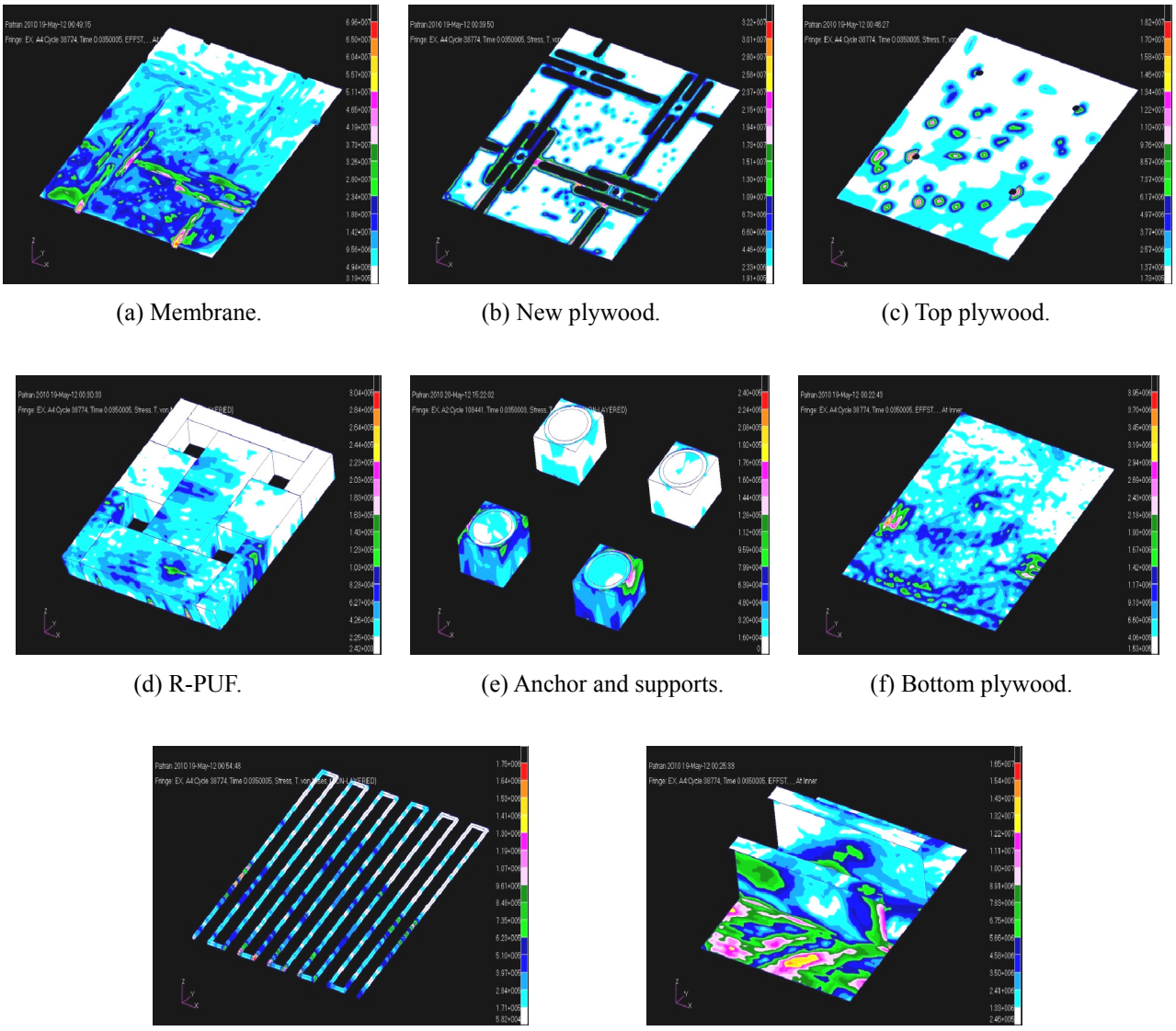

(a) Membrane. (b) New plywood. (c) Top plywood.

(d) R-PUF. (e) Anchor and supports. (f) Bottom plywood.

(g) Mastic. (h) Hull.

Fig. 19 Effective stress contour of KC-1 model Case B.

Table 2 Maximum effective stress at 35 *ms* (local time) and 4010.035 *sec* (global time) (Unit: *MPa*).

	Case A	Case B	Error (%) (criterion: Case A)
Membrane	69.6	72.7	4.45
New plywood	29.7	32.2	8.42
Top plywood	17.3	18.2	5.20
R-PUF	0.29	0.30	3.45
Anchor and supports	0.24	0.25	4.17
Bottom plywood	3.83	3.95	3.13
Mastic	1.71	1.75	2.34
Hull	16.1	16.5	2.48
Average Error			4.21

Table 3 Computational time for Case A and Case B.

	Case A		Case B	
	Global analysis	Local analysis	Global analysis	Local analysis
Total number of elements	92937	61339	91273	59675
Time period of observation (*sec*)	4014	0.05	4014	0.05
Averaged time step size (*sec*)	3.598E-03	9.370E-07	3.598E-03	9.370E-07
Total number of iterations	1,115,508	55,342	1,115,508	55,342
Total CPU time (*hr.*)	9.73	89.66	9.73	2.54

CONCLUDION REMARKS

In this study, the sloshing resistance performance for the KC-1 type LNG carrier insulation system was evaluated by FSI analysis. The research results are listed below.

(1) FSI analysis was carried out based on the well-known arbitrary Lagrangian-Eulerian method, and other novel techniques for FSI analysis were introduced.
(2) The flow velocity, pressure, and volume fraction of the internal LNG of the KC-1 insulation system can be calculated during the sufficient sloshing time based on the global analysis method. The obtained values are mapped into the local FE model of the KC-1 insulation system.
(3) The maximum effective stress contours can be calculated based on the local analysis method. During local analysis, the arbitrary Lagrangian-Eulerian method based FSI analysis is adopted. Moreover, a novel element model, i.e, additional thickness model without contact element, was implemented into the local KC-1 insulation system in order to remarkably reduce the computational time and cost.
(4) Although validation of the analysis results through a comparison of the experiments was not carried out, the proposed analysis technique can potentially be used as a robust integrity assessment technique for LNG carrier's insulation systems.

ACKNOWLEDGEMENTS

This work was supported by a National Research Foundation of Korea (NRF) grant funded by the Korean government (MEST) through GCRC-SOP.

REFERENCES

Beckert, A., 2003. Coupling fluid (CFD) and structural (FE) models using finite interpolation elements. *Aerospace Science and Technology*, 4(1), pp.13-22.

Cho, J.R. and Lee, S.Y., 2003. Dynamic analysis of baffled fuel-storage tank using the ALE finite element method. *International Journal of Numerical Methods in Fluids*, 41(2), pp.185-208.

Cho, J.R. and Lee, H.W., 2004. Non-linear finite element analysis of large amplitude sloshing flow in two-dimensional tank. *International Journal for Numerical Methods in Engineering*, 61(4), pp.514-531.

Cho, J.R., Lee, H.W., Sohn, J.S., Kim, G.J. and Woo, J.S., 2006. Numerical investigation of hydroplaning characteristics of three-dimensional patterned tire. *European Journal of Mechanics A/Solids*, 25(6), pp.914-926.

Cho, J.R., Lee, H.W. and Yoo, W.S., 2007. A wet-road braking distance estimate utilizing the hydroplaning analysis of patterned tire. *International Journal for Numerical Methods in Engineering*, 69(7), pp.1423-1445.

Cho, J.R., Park, S.W., Kim, H.S. and Rashed, S., 2008. Hydroelastic analysis of insulation containment of LNG carrier by global-local approach. *International Journal for Numerical Methods in Engineering*, 76(5), pp.749-774.

Faltinsen, O.M. and Timokha, A.N., 2009. *Sloshing*. Cambridge University Press.

Farhat, C., Lesoinne, M. and LeTallec, P., 1998. Load and motion transfer algorithms for fluid/structure interaction problems with non-matching discrete interfaces: momentum and energy conservation, optimal discretization and application to aeroelasticity. *Computer Methods in Applied Mechanics and Engineering*, 157(1-2), pp.95-114.

Harder, R.L. and Desmarais, R.N., 1972. Interpolation using surface splines. *Journal of Aircraft*, 9(2), pp.189-191.

Hirt, C.W. and Nichols, J.E., 1981. Volume of fluid method for the dynamic of free boundaries. *Journal of Computational Physics*, 39, pp.201-225.

Hu, N., 1997. A solution method for dynamic contact problems. *Computers & Structures*, 63(6), pp.1053-1063.

Mao, K.M. and Sun, C.T., 1991. A refined global-local finite element analysis method. *International Journal for Numerical Methods in Engineering*, 32(1), pp.29-43.

Morand, H.J.P. and Ohayon, R., 1995. *Fluid structure interaction*. Wiley & Sons.

Mote, C.D., 1971. Global-local finite element. *International Journal for Numerical Methods in Engineering*, 3(4), pp.565-574.

Nakayama, T. and Washizu, K., 1980. Nonlinear analysis of liquid motion in a container subjected to forced pitching oscillation. *International Journal for Numerical Methods in Engineering*, 15(8), pp.1207-1220.

Patankar, S.V., 1980. *Numerical heat transfer and fluid flow*. McGraw-Hill.

Schäfer, M. and Teschauer, I., 2001. Numerical simulation of coupled fluid-solid problems. *Computer Methods in Applied Mechanics and Engineering*, 190(28), pp.3645-3667.

Sigrist, J.F. and Abouri, D., 2006. Numerical simulation of a non-linear coupled fluid-structure problem with implicit and explicit coupling procedure. *ASME Conference Proceeding Volume 9: 6th FSI, AE and FIV and N Symposium, PVP 2006-ICPVT-11-93107*. 23-27 July 2006, pp.99-106.

Valtinsen, O.M., 1974. A nonlinear theory of sloshing in rectangular tanks. *Journal of Ship Research*, 18(4), pp.224-241.

Wu, G.X., Ma, Q.W. and Taylor, R.E., 1998. Numerical simulation of sloshing waves in a 3D tank based on a finite element method. *Applied Ocean Research*, 20, pp.337-355.

Zienkiewicz, O.C., Taylor, R.L. and Zhu, J.Z., 2005. *The finite element method: Its basis and fundamentals*. Butterworth-Heinemann.